ISSN: 2181-3337 | SCIENTISTS.UZ VOLUME 5 ISSUE 7 JULY 2026

# INFLUENCE OF DEFECTS ON THE ELECTRICAL CONDUCTIVITY OF $SB_xSE_\gamma$ THIN FILMS PREPARED BY THE INDEPENDENT SOURCE VAPOR TRANSPORT TECHNIQUE

**K.M. Quchqarov[1], B.A. Ergashev[1], M.P. Pirimmatov[1], A.S. Matmuratov[1]*, B.A. Gulumbaev[1], X.Z.To'liboyeva[1]**

[1]S.A. Azimov Physics-Technical Institute, Academy of Sciences of the Republic of Uzbekistan, 2B Chingz Aitmatov Street, Tashkent 100084, Uzbekistan.

*Corresponding author: e-mail: matmuratovajdos@gmail.com

**DOI: 10.67620/sai.57a0004**

## ABSTRACT

*In this study, the structural and electrophysical properties of SbxSey thin films grown at different source temperatures using the independent-source vapor transport method were investigated. The composition of the thin films was determined by energy-dispersive X-ray spectroscopy (EDS), revealing that as the source temperature increases, the Sb/Se atomic ratio shifts from Se-rich to Sb-rich. Specifically, a Se-rich composition (Sb/Se ≈ 0.51) was observed in films obtained at 500 °C, a stoichiometric composition (Sb/Se ≈ 0.67) at 525 °C, and an Sb-rich composition (Sb/Se ≈ 0.82) at 550 °C. The temperature dependence of electrical conductivity was measured using a cryostat, and activation energies were calculated from Arrhenius analysis. According to the results, the following activation energies were identified for the corresponding samples: $E_v$ + 0.578 eV for the 500 °C film, $E_v$ + 0.111 eV for the 525 °C film, and E□ − 0.518 eV for the 550 °C film.*

## ACCEPTED

**31.07.26**

***Keywords:*** *independent-source vapor transport deposition, $Sb_2Se_3$ thin-film solar cells, substrate preparation, source temperature effect, point defects, electrical conductivity, activation energy, photovoltaic absorber materials.*

CC BY

## 1. INTRODUCTION

The growing global demand for energy underscores the need for stable, reliable, and economically efficient photovoltaic materials. Currently, solar cells using polycrystalline silicon (Si), cadmium telluride (CdTe), and copper–indium–gallium selenide (CIGS; $Cu(In,Ga)Se_2$) serve as primary absorber materials, achieving power conversion efficiencies (PCE) above 20% (Green et al., 2021; Mavlonov et al., 2020; Scheer & Schock, 2011). However, the high processing cost of Si, the toxicity of Cd, and the high cost and scarcity of Ga, In, and Te pose significant challenges to large-scale thin-film solar cell production using these materials(Scheer & Schock, 2011; Zakutayev, 2017). Kesterite-based solar cells ($Cu_2ZnSn(S_xSe_{1-x})_4$, CZTS/Se) achieved a maximum efficiency of approximately 12.7% in 2021 (J. Zhou et al., 2021), but further improvements have stagnated due to defects arising from the material's complex chemical structure. Halide perovskites ($CH_3NH_3PbI_3$) have recently achieved efficiencies near 25%(Green et al., 2021). Nevertheless, the instability and toxicity of Pb-based perovskites limit their use as absorber layers in long-

term, environmentally sustainable photovoltaic devices, pointing to the need for alternative absorber materials (Hobson, Hutter, et al., 2020; Zakutayev, 2017).

To overcome these problems, recent scientific research has focused on antimony selenide ($Sb_2Se_3$) chalcogenide-based thin films as promising absorber layers for solar cells. This compound has attracted considerable interest as a potential absorber material in photovoltaic devices due to its p-type conductivity, high optical absorption coefficient in the visible spectral range ($10^5$ $cm^{-1}$), band gap in the range of 1.1–1.3 eV, high charge mobility (10 $cm^2$ $V^{-1}s^{-1}$), low toxicity, simple crystal structure, low cost, and the abundance of its constituent elements in nature (Chen, Bobela, et al., 2017; Ghosh et al., 2020; Hutter et al., 2018; Lei et al., 2019; Y. Zhou et al., 2014).

Unlike conventional absorbers, $Sb_2Se_3$ possesses a unique quasi-one-dimensional (Q1D) structure composed of $[Sb_4Se_6]_n$ ribbons, which are held together by van der Waals forces without dangling bonds, while Sb–Se atoms within the ribbons are covalently bonded (Lei et al., 2019). However, first-principles calculations have shown that the interactions between crystal ribbons in $Sb_2Se_3$ lie between van der Waals and covalent bonding (X. Wang et al., 2022). Other studies have demonstrated that aligning the growth orientation of $[Sb_4Se_6]_n$ ribbons perpendicular to the substrate along the [211] and [221] crystal planes reduces the density of unsatisfied bonds and forms naturally benign grain boundaries (Hutter et al., 2018; Kondrotas et al., 2019; Z. Li et al., 2019; L. Wang et al., 2017). Nevertheless, crystal ribbons oriented along the [001] plane significantly suppress non-radiative recombination losses, hence enhancing the efficiency of $Sb_2Se_3$ polycrystalline thin films in photovoltaic (PV) devices (Williams et al., 2020; Y. Zhou et al., 2015). For most known inorganic absorbers (such as Si, CIGS, and CdTe), the breakage of covalent bonds inevitably introduces defect states and recombination centers at the grain boundaries, which can effectively block charge collection and potentially reduce device efficiency during the interface recombination. Contrastingly, $Sb_2Se_3$ has intrinsically benign grain boundaries which could therefore offer a sustainable solution to drawbacks associated with traditional absorber materials if efficiency values continue to rise(Wijesinghe et al., 2023).

Three main areas of research within the field currently are control of the orientation of $Sb_2Se_3$ films(Hutter et al., 2018; Kondrotas et al., 2019; Z. Li et al., 2019; L. Wang et al., 2017), band alignment optimization(Gharibshahian et al., 2020; G. Li et al., 2019; Shiel et al., 2020; Wen et al., 2017), and defect passivation at interfaces/surfaces to suppress recombination losses and the open-circuit voltage (VOC) deficit (Chen, Wang, et al., 2017; Hobson, Phillips, et al., 2020; Huang et al., 2019; Liang et al., 2020; Ma et al., 2020). Despite the excellent properties of $Sb_2Se_3$, PCE values are still far below the maximum theoretical value of 30% predicted by the Shockley–Queisser (S–Q) model (Shockley & Queisser, 1961). Spectroscopic limited maximum efficiency (SLME) calculations show that $Sb_2Se_3$ has substantial potential for the development of highly efficient solar cells with an upper limit of 30%, which is actually higher than both CdTe and CZTS/Se (Phillips et al., 2019).

Alongside various technologies for fabricating $Sb_2Se_3$-based thin-film solar cells, vapor-phase deposition methods have been actively studied. In particular, vapor transport deposition (VTD) has been shown to enable the growth of $Sb_2Se_3$ thin films with vertically oriented one-dimensional crystal structures on the substrate. Initial studies using this method achieved efficiencies of 5–6% in solar cells (Y. Zhou et al., 2015). Subsequent research reported that optimization of process parameters increased the efficiency of $Sb_2Se_3$-based solar cells prepared by the VTD method to 7–8% (Dong et al., 2021; X. Wang et al., 2018).

This study thoroughly analyzes the effects of source temperature and defect conditions on the electrical conductivity of $Sb_2Se_3$ thin films synthesized via independent-source vapor transport deposition.

**2. Experimental section**

$Sb_xSe_y$ thin films were systematically grown at various source temperatures using the independent-source vapor transport method. Initially, soda-lime glass (SLG) substrates measuring 2×2 cm were selected. To ensure optimal film quality, substrates underwent a multi-step cleaning process: chemical


ISSN: 2181-3337 | SCIENTISTS.UZ

cleaning with acetone and ethanol, ultrasonic treatment for 10 minutes, and drying under a nitrogen gas flow. Subsequently, molybdenum (Mo) thin films approximately 1 μm thick were deposited onto glass substrates under high-vacuum conditions via magnetron sputtering. The deposition was conducted at a pressure of $10^{-5}$ torr in an argon (Ar) atmosphere with a power of 120 W. The Mo layer functioned as the electrical contact and back electrode. $Sb_xSe_y$ thin films were then deposited onto the prepared glass/Mo structures using the independent-source vapor transport deposition method. The thin-film growth process was tightly controlled. Glass and glass/Mo substrates (2×2 cm) were placed in graphite holders, permitting free rotation around a horizontal axis. An initial vacuum of 1.3 Pa ($10^{-2}$ mmHg) was established using a mechanical pump, followed by the introduction of argon (Ar) gas to achieve an inert atmosphere at 7 Pa. The system was heated externally, and once the substrate temperature reached 400 °C, source temperatures of 500 °C, 525 °C, and 550 °C were applied to achieve thin-film growth. Each deposition lasted 10 minutes, with substrate rotation at 2 $min^{-1}$, yielding uniform $Sb_2Se_3$ thin films of consistent thickness.

The chemical composition of the thin films was determined using energy-dispersive spectroscopy (EDS, AzTec Advanced, Oxford Instruments), enabling assessment of elemental ratios and the influence of source temperature on composition. Morphology and thickness were examined with a scanning electron microscope (SEM, JEOL JSM-IT510). As the source temperature increased, the mass of evaporated $Sb_2Se_3$ increased, yielding film thicknesses between approximately 1.7 μm and 6.3 μm (Table 1).

The electrophysical properties of the samples were investigated by measuring the temperature dependence of electrical conductivity in a cryostat. High-precision electrical measurements were conducted with the SM2460 SourceMeter (Keithley, USA). The results were analyzed using the Arrhenius equation to calculate the activation energies of charge carriers.

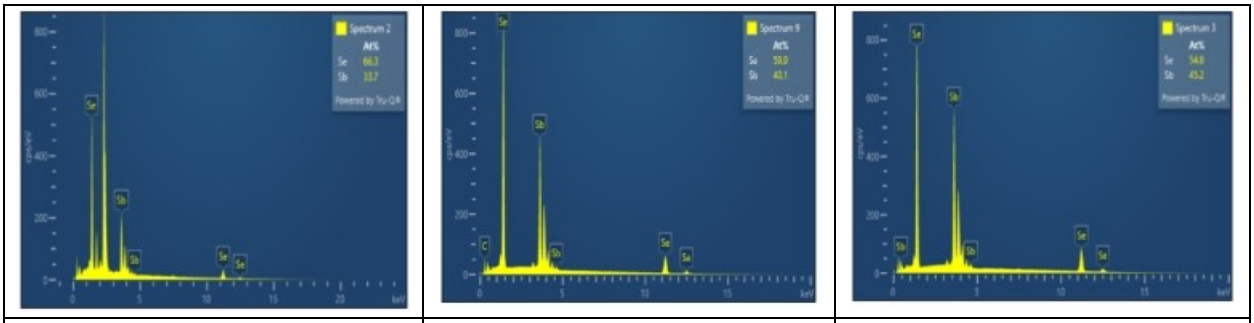
**3. Results and discussion**

Analysis of energy-dispersive spectroscopy (EDS) results (Figure 1) revealed that changes in source temperature impacted the selenium (Se) content of the obtained thin films (Table 1). As shown in the EDS spectra presented in Figures 1a, b, and c, the primary energy peaks corresponding to Sb and Se elements were clearly observed for all samples. Table 1 presents the EDS results for samples grown at different source temperatures, along with their thicknesses determined by scanning electron microscopy (SEM).

Table 1 shows that, at a constant substrate temperature, increasing the source temperature decreases Se content and increases film thickness in $Sb_xSe_y$ thin films. This phenomenon can be explained by several basic physical factors. First, the evaporation process of the initial $Sb_2Se_3$ binary compound is non-stoichiometric, due to the significant difference in vapor pressures of Sb and Se:Se is highly volatile, and its vapor pressure increases rapidly with temperature, whereas Sb is relatively less volatile. At lower source temperatures, the vapor phase contains a higher proportion of Se, resulting in Se-rich or near-Se-rich thin films. When the source temperature reaches an optimal value, the evaporation, transport, and condensation processes of Sb and Se atoms achieve equilibrium, resulting in stoichiometric $Sb_2Se_3$ thin films.

At higher source temperatures, kinetic processes control the system. The evaporation speed of Se atoms increases sharply, leading some to disperse into the vapor phase or re-evaporate from the substrate surface before sufficient bonding occurs. Meanwhile, Sb atoms, being heavier and more strongly bonded to the crystal lattice, condense more effectively on the substrate surface. Consequently, despite constant substrate temperature, thin films grown at higher source temperatures exhibit Sb-rich composition.


ISSN: 2181-3337 | SCIENTISTS.UZ



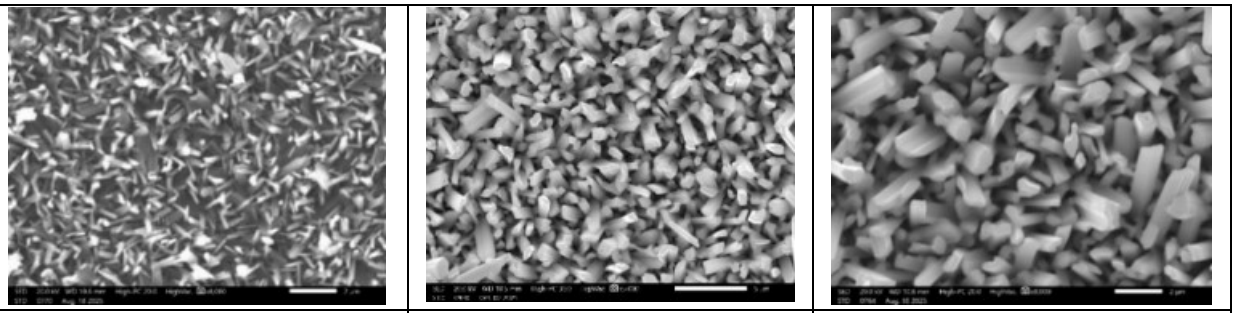
| t=500 ºC | t=525 ºC | t=550 ºC |
|---|---|---|

***Figure 1.*** *Energy-dispersive X-ray spectroscopy (EDS) analysis of $Sb_xSe_y$ thin films grown at different source temperatures. (a–c) Elemental composition of the thin films prepared at source temperatures of 500, 525, and 550 °C, respectively.*

***Table 1.*** *Elemental composition determined by EDS for $Sb_xSe_y$ thin films grown at different source temperatures.*

| № | Substrate Temperature (ºC) | Source Temperature (ºC) | Evaporated Source mass(mg) | Film Thickness (μm) | Composition | | |
|---|---|---|---|---|---|---|---|
| | | | | | Sb (%) | Se (%) | Sb/Se |
| M54 | 400 | 500 | 143,6 | 1,732 | 33,7 | 66,3 | 0,5083 |
| M55 | | 525 | 224,2 | 3,276 | 40,1 | 59,9 | 0,6694 |
| M53 | | 550 | 363,6 | 6,291 | 45,2 | 54,8 | 0,8248 |

With increasing source temperature, the observed increase in the thickness of $Sb_2Se_3$ thin films (Table 1) can be explained by the thermodynamic and kinetic characteristics of the evaporation process. As the source temperature rises, the evaporation rate of $Sb_2Se_3$ and the density of the vapor-phase material flux increase, leading to more material reaching and condensing on the substrate surface. Since the substrate temperature remains constant, at higher source temperatures, the vapor flux leads to greater material accumulation over a shorter time, thereby producing thicker films. Consequently, a consistent increase in film thickness with rising source temperature was observed.



| a) **500 ºC** | b) **525 ºC** | c) **550 ºC** |
|---|---|---|

***Figure 2.*** *Scanning electron microscopy (SEM) surface morphology of $Sb_2Se_3$ thin films deposited at different source temperatures: (a) 500 °C, (b) 525 °C, and (c) 550 °C.*

Figures 2a–c present the SEM images of $Sb_2Se_3$ thin films deposited on Mo-coated glass substrates at different source temperatures using the independent-source vapor transport method. The surface morphology changes significantly with increasing source temperature. The film deposited at 500 °C consists of densely packed, fine rod-like grains with relatively small grain size and random orientation. Increasing the source temperature to 525 °C promotes grain growth, resulting in larger, more compact grains with improved surface coverage and reduced porosity. At 550 °C, further grain coarsening is observed, and the grains become noticeably larger with well-defined faceted morphology. The enhanced



ISSN: 2181-3337 | SCIENTISTS.UZ

grain size and improved grain connectivity indicate increased surface diffusion and adatom mobility at higher source temperatures, leading to better crystallization and reduced grain boundary density.
In the films deposited at different source temperatures (500 °C, 525 °C, and 550 °C), the crystals exhibit a nanorod-like morphology. It was determined that, with increasing source temperature, the length of the nanorods increases from approximately 0.3 μm to ~2 μm.

One of the main reasons for this behavior is the variation in film thickness under different growth conditions. The samples obtained at a source temperature of 500 °C are relatively thin, and the crystalline grains have not yet fully developed. As the temperature increases, the film becomes thicker, which promotes grain growth and leads to the formation of larger crystalline domains.

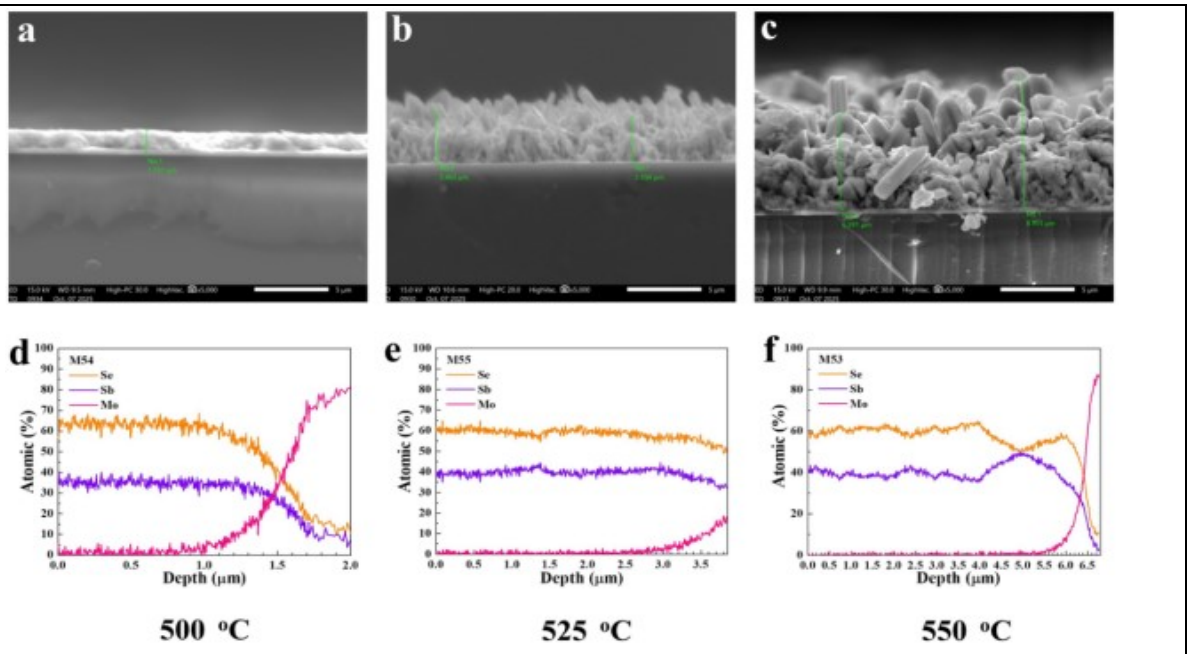



***Figure 3.*** *Cross-sectional (SEM) images (a–c) and thickness-dependent compositional (EDS) analysis (d–f) of $Sb_xSe_y$ thin films deposited at different source temperatures.*

Figure 3 presents the cross-sectional SEM micrographs (Fig. 3a–c) and the corresponding EDS depth profiles (Fig. 3d–f) of $Sb_2Se_3$ thin films deposited on Mo-coated glass substrates under different source temperatures. The results clearly demonstrate that the source temperature markedly influences the growth kinetics of the absorber layer, leading to significant changes in film thickness, grain morphology, crystallographic growth orientation, and compositional uniformity.

The Se-rich sample deposited at 500 °C (Fig. 3a) exhibits the smallest thickness (≈2 μm) and consists of fine grains with an average size of approximately 0.3 μm. Most crystallites are oriented nearly parallel to the substrate surface, suggesting that crystal growth is dominated by lateral nucleation rather than vertical grain propagation. Such a morphology is characteristic of insufficient surface diffusion, where the kinetic energy of arriving Sb and Se species is too low to overcome diffusion barriers. Consequently, numerous nucleation centers are formed, suppressing competitive grain growth and producing a dense microstructure with a high density of grain boundaries. Since grain boundaries are known to act as trapping and recombination centers, this morphology is generally unfavorable for efficient carrier transport in photovoltaic absorbers.

When the source temperature is increased to 525 °C, forming the stoichiometric sample (Fig. 3b), the microstructure undergoes a pronounced transformation. The film thickness increases to approximately 4 μm, while the average grain size reaches about 1 μm. More importantly, the crystallites become preferentially aligned perpendicular to the substrate, resulting in a highly ordered columnar structure extending throughout the entire absorber layer. This transition reflects enhanced surface diffusion of adatoms and increased atomic mobility, allowing neighboring nuclei to merge through competitive grain


ISSN: 2181-3337 | SCIENTISTS.UZ

growth. Under these conditions, grains with energetically favorable orientations outgrow surrounding crystallites, reducing the overall grain-boundary density. Such vertically aligned columnar grains provide continuous conduction pathways across the absorber thickness, thereby facilitating charge-carrier collection and reducing recombination losses. Similar microstructural evolution has been widely reported as a prerequisite for achieving high-performance $Sb_2Se_3$ photovoltaic devices.

Further increasing the source temperature to 550 °C leads to the formation of the Sb-rich sample (Fig. 3c), where the film thickness reaches approximately 6.5 μm and the average grain size increases to nearly 3 μm. Although grain growth is significantly promoted, the columnar morphology becomes less ordered and many crystallites are inclined with respect to the substrate normal. The larger grains indicate accelerated diffusion and grain coalescence; however, excessive thermal energy simultaneously enhances selenium re-evaporation because of its relatively high vapor pressure compared with antimony. The resulting deviation from stoichiometry modifies the local supersaturation during film growth, promoting anisotropic crystal growth and increasing structural disorder. Consequently, the film exhibits a rougher morphology and less uniform grain orientation despite its larger crystal size. This observation suggests that grain enlargement alone is insufficient to guarantee improved structural quality, as crystallographic alignment and compositional stability are equally important.

The EDS compositional depth profiles (Fig. 3d–f) further corroborate these structural observations. In the Se-rich sample, the selenium concentration remains consistently higher than that of antimony across the entire film thickness, confirming the Se-rich growth condition. In contrast, the stoichiometric sample exhibits nearly constant Sb and Se concentrations throughout the absorber layer, indicating excellent compositional homogeneity and nearly stoichiometric composition. Such uniform elemental distribution suggests stable evaporation kinetics and balanced incorporation of both constituent elements during deposition. Conversely, the Sb-rich sample contains a higher Sb concentration accompanied by slight compositional fluctuations along the growth direction. These fluctuations most likely originate from the preferential evaporation of selenium at elevated source temperatures, which has frequently been reported as a principal challenge in the high-temperature growth of $Sb_2Se_3$ thin films.

The combined SEM and EDS analyses reveal that the evolution of the $Sb_2Se_3$ microstructure is governed by the competition between surface diffusion, nucleation density, and selenium volatilization. At low source temperatures, limited atomic mobility results in numerous nuclei and fine-grained, compact films. Increasing the source temperature enhances adatom diffusion, promoting columnar grain growth and improved crystallinity. However, excessively high temperatures accelerate selenium loss, disturb the stoichiometric balance, and induce structural disorder despite continued grain coarsening.

To evaluate the electrical properties of $Sb_xSe_y$ thin films, their specific electrical conductivity was first measured at room temperature using the “sandwich” method. The results are summarized in Table 2. According to the experimental data, the lowest conductivity value was observed in the stoichiometric sample. This behavior is explained by the fact that the stoichiometric $Sb_2Se_3$ thin film exhibits electrical properties characteristic of an intrinsic semiconductor. It is well known that intrinsic semiconductors have a low concentration of free charge carriers, which considerably reduces their electrical conductivity compared to doped semiconductors (Streetman & Banerjee, 2015; Sze & Ng, 2006; X. Wang et al., 2018).

Measurements performed using the hot-probe method revealed that Sb-rich samples show strong n-type conductivity, while Se-rich samples show p-type conductivity. The stoichiometric sample demonstrated weak p-type conductivity (Table 2). These results show that the ratio of Sb and Se atoms is directly related to defect centers in the crystal lattice and the nature of charge carriers (Streetman & Banerjee, 2015).

To gain a better understanding of point defects in the samples, the temperature dependence of electrical conductivity was measured over 77–300 K using a cryostat and the Van der Pauw method. The


ISSN: 2181-3337 | SCIENTISTS.UZ

experimental results were expressed through an Arrhenius-type exponential relationship characteristic of semiconductors (Moynihan et al., 1982):

$$\sigma(T)=\sigma_0 \cdot e^{-\frac{E_a}{kT}} \qquad (1)$$

where σ is the dark specific conductivity, σ0 is the pre-exponential factor, $E_a$ is the activation energy for conductivity, k is the Boltzmann constant, and T is the absolute temperature.

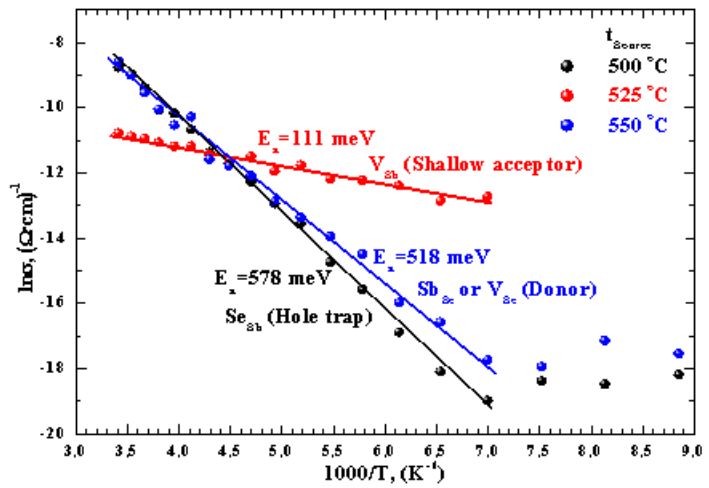



***Figure 4.*** *Arrhenius plots used to determine the activation energy from the temperature dependence of the electrical conductivity of the samples.*

Figure 4 presents the Arrhenius plots for samples obtained at different source temperatures. Based on these plots, the activation energies for each sample were determined. The calculated Ea values were 578 meV, 111 meV, and 518 meV for samples grown at source temperatures of 500 °C, 525 °C, and 550 °C, respectively (Table 2). The obtained results are in good agreement with values reported in the literature for $Sb_2Se_3$ thin films (Hobson, Phillips, et al., 2020; Huang et al., 2019; Liu et al., 2017; Savory & Scanlon, 2019; Wijesinghe et al., 2023).

For the Se-rich sample, the identified activation energy of ($E_a=E_v+0.578$ eV) corresponds to a defect state associated with Se atoms occupying Sb lattice sites ($Se_{Sb}$). Such antisite defects generate "hole-trap" levels that act as trapping centers for holes. Under Se-rich conditions, i.e., when $\mu_{Se}$ is high, $Se_{Sb}$ antisite defects become the lowest-energy acceptor defects (Hobson, Phillips, et al., 2020; Huang et al., 2019, 2021; Liu et al., 2017; Savory & Scanlon, 2019; Wijesinghe et al., 2023). According to density functional theory (DFT) calculations, Se vacancies and compound-defect clusters can form deep energy levels far from the conduction band, thereby limiting the ionization of charge carriers (Chen, Bobela, et al., 2017). The literature reports that under Se-rich conditions, the probability of forming $Se_{Sb}$ antisite defects increases with increasing Sb vacancy ($V_{Sb}$) concentration. In particular, $Se_{Sb}$ antisite defects generate deep energy levels near the mid-gap, acting as efficient recombination centers. As a result, the ionization of charge carriers is restricted, thereby reducing electrical conductivity (Hobson, Phillips, et al., 2020; Huang et al., 2019; Savory & Scanlon, 2019; Wijesinghe et al., 2023).

For the Sb-rich sample, the activation energy of ($E_a=E_c-0.518$ eV) was identified, which can be ascribed to Sb atoms occupying Se lattice sites ($Sb_{Se}$) or the formation of Se vacancies ($V_{Se}$). These defects generate donor-type levels, thereby increasing the electron concentration. As a result, the sample shows n-type electrical conductivity. Under Se-poor conditions, i.e., when $\mu_{Se}$ is low, three $Sb_{Se}$ antisite defects represent the lowest-energy acceptor defects, while three $V_{Se}$ vacancy defects act as the lowest-energy donor defects. Consequently, strong donor–acceptor compensation occurs (Hobson, Phillips, et al., 2020;


ISSN: 2181-3337 | SCIENTISTS.UZ

Huang et al., 2019, 2021; Liu et al., 2017; Savory & Scanlon, 2019; Wijesinghe et al., 2023). The literature reports that under Sb-rich conditions, donor-type defects such as Se vacancies ($V_{Se}$) and Sb antisite defects ($Sb_{Se}$) are energetically favored. Some of these defects form shallow levels near the conduction band, which can ionize even at low temperatures. As a result, the electron concentration increases and electrical conductivity increases (Hobson, Phillips, et al., 2020; Huang et al., 2019; Savory & Scanlon, 2019; Wijesinghe et al., 2023).

For the stoichiometric sample, a relatively small activation energy of ($E_a$=$E_v$+0.111 eV) was observed. This corresponds to shallow acceptor levels associated with Sb vacancies ($V_{Sb}$). Such defects increase hole concentration, thereby enhancing p-type conductivity, and are considered beneficial from the perspective of electrical properties (Hobson, Phillips, et al., 2020; Huang et al., 2019, 2021; Liu et al., 2017; Savory & Scanlon, 2019; Wijesinghe et al., 2023).

Overall, the activation energy values indicate that deep-level defects dominate in Se-rich and Sb-rich samples, whereas shallow acceptor states are primarily present in the stoichiometric sample.(Hobson, Phillips, et al., 2020; Huang et al., 2019; Savory & Scanlon, 2019; Wijesinghe et al., 2023)

***Table 2.*** *Electrophysical Properties and Defect Characteristics of $Sb_xSe_y$ Thin Films*

| Sample | Sb/Se | Type | σ (Ω×m)$^{-1}$ | $E_a$ (eV) | Defect type | Defect | References |
|---|---|---|---|---|---|---|---|
| **M54** | 0,5083 | p | $6,57\times10^{-5}$ | $E_v$ + 0,578 | Hole-trap | $Se_{Sb}$ | 24-29 |
| **M55** | 0,6694 | ~p | $1,14\times10^{-5}$ | $E_v$ + 0,111 | Shallow acceptor | $V_{Sb}$ | 24-29 |
| **M53** | 0,8248 | n | $1,89\times10^{-4}$ | $E_c$ – 0,518 | Donor | $Sb_{Se}$ or $V_{Se}$ | 24-27 |

## 4. Conclusion

In conclusion, the composition of $Sb_2Se_3$ thin films prepared by the independent-source vapor transport method shifts from Se-rich to Sb-rich as the source temperature increases. At a source temperature of 525 °C, a stoichiometric thin film was formed and exhibited distinct electrical properties. The conductivity of the samples varied from $1.14\times10^{-5}$ $(\Omega\cdot\ m)^{-1}$ to $1.89\times10^{-4}$ $(\Omega\cdot\ m)^{-1}$ as the Se content increased. Activation energies determined from specific electrical conductivity tests indicated the presence of deep-level defects in Sb-rich and Se-rich samples, while shallow acceptor defects were observed in the stoichiometric sample. In the Sb-rich sample, the type of electrical conductivity changed from p-type to n-type. In contrast, in the stoichiometric sample, the increased hole concentration increased p-type conductivity, which is considered advantageous for electrical properties. The obtained results show the potential of $Sb_2Se_3$ thin films for the fabrication of high-efficiency solar cells.

**Funding**

This work was supported by the Belarusian Republican Foundation for Fundamental Research (Grant No. F25UZBG-109).

## REFERENCES

1. Chen, C., Bobela, D. C., Yang, Y., Lu, S., Zeng, K., Ge, C., Yang, B., Gao, L., Zhao, Y., Beard, M. C., & Tang, J. (2017). Characterization of basic physical properties of Sb2Se3 and its relevance for photovoltaics. Frontiers of Optoelectronics, 10(1), 18–30. https://doi.org/10.1007/s12200-017-0702-z
2. Chen, C., Wang, L., Gao, L., Nam, D., Li, D., Li, K., Zhao, Y., Ge, C., Cheong, H., Liu, H., Song, H., & Tang, J. (2017). 6.5% Certified Efficiency Sb 2 Se 3 Solar Cells Using PbS Colloidal Quantum Dot Film as Hole-Transporting Layer. ACS Energy Letters, 2(9), 2125–2132. https://doi.org/10.1021/acsenergylett.7b00648
3. Dong, J., Liu, Y., Wang, Z., & Zhang, Y. (2021). Boosting V OC of antimony chalcogenide solar cells: A review on interfaces and defects. Nano Select, 2(10), 1818–1848. https://doi.org/10.1002/nano.202000288

4. Gharibshahian, I., Orouji, A. A., & Sharbati, S. (2020). Towards high efficiency Cd-Free Sb2Se3 solar cells by the band alignment optimization. Solar Energy Materials and Solar Cells, 212, 110581. https://doi.org/10.1016/j.solmat.2020.110581
5. Ghosh, S., Moreira, M. V. B., Fantini, C., & González, J. C. (2020). Growth and optical properties of nanocrystalline Sb2Se3 thin-films for the application in solar-cells. Solar Energy, 211, 613–621. https://doi.org/10.1016/j.solener.2020.10.001
6. Green, M., Dunlop, E., Hohl-Ebinger, J., Yoshita, M., Kopidakis, N., & Hao, X. (2021). Solar cell efficiency tables (version 57). Progress in Photovoltaics: Research and Applications, 29(1), 3–15. https://doi.org/10.1002/pip.3371
7. Hobson, T. D. C., Hutter, O. S., Fleck, N., Daniels, L. M., Major, J. D., Ng, T. M., & Durose, K. (2020). Vegard Relation and Raman Band Reference Data Generated from Bulk Crystals of Kesterite-Phase Composition Series Cu 2 ZnSnS 4 x Se 4–4 x (CZTSSe, $0 \leq x \leq 1$). Crystal Growth & Design, 20(4), 2164–2173. https://doi.org/10.1021/acs.cgd.9b00911
8. Hobson, T. D. C., Phillips, L. J., Hutter, O. S., Durose, K., & Major, J. D. (2020). Defect properties of Sb2Se3 thin film solar cells and bulk crystals. Applied Physics Letters, 116(26). https://doi.org/10.1063/5.0012697
9. Huang, M., Cai, Z., Wang, S., Gong, X., Wei, S., & Chen, S. (2021). More Se Vacancies in Sb 2 Se 3 under Se-Rich Conditions: An Abnormal Behavior Induced by Defect-Correlation in Compensated Compound Semiconductors. Small, 17(36), 2102429. https://doi.org/10.1002/smll.202102429
10. Huang, M., Xu, P., Han, D., Tang, J., & Chen, S. (2019). Complicated and Unconventional Defect Properties of the Quasi-One-Dimensional Photovoltaic Semiconductor Sb 2 Se 3. ACS Applied Materials & Interfaces, 11(17), 15564–15572. https://doi.org/10.1021/acsami.9b01220
11. Hutter, O. S., Phillips, L. J., Durose, K., & Major, J. D. (2018). 6.6% efficient antimony selenide solar cells using grain structure control and an organic contact layer. Solar Energy Materials and Solar Cells, 188, 177–181. https://doi.org/10.1016/j.solmat.2018.09.004
12. Kondrotas, R., Zhang, J., Wang, C., & Tang, J. (2019). Growth mechanism of Sb2Se3 thin films for photovoltaic application by vapor transport deposition. Solar Energy Materials and Solar Cells, 199, 16–23. https://doi.org/10.1016/j.solmat.2019.04.024
13. Lei, H., Chen, J., Tan, Z., & Fang, G. (2019). Review of Recent Progress in Antimony Chalcogenide-Based Solar Cells: Materials and Devices. Solar RRL, 3(6). https://doi.org/10.1002/solr.201900026
14. Li, G., Li, Z., Liang, X., Guo, C., Shen, K., & Mai, Y. (2019). Improvement in Sb 2 Se 3 Solar Cell Efficiency through Band Alignment Engineering at the Buffer/Absorber Interface. ACS Applied Materials & Interfaces, 11(1), 828–834. https://doi.org/10.1021/acsami.8b17611
15. Li, Z., Liang, X., Li, G., Liu, H., Zhang, H., Guo, J., Chen, J., Shen, K., San, X., Yu, W., Schropp, R. E. I., & Mai, Y. (2019). 9.2%-efficient core-shell structured antimony selenide nanorod array solar cells. Nature Communications, 10(1), 125. https://doi.org/10.1038/s41467-018-07903-6
16. Liang, G.-X., Luo, Y.-D., Chen, S., Tang, R., Zheng, Z.-H., Li, X.-J., Liu, X.-S., Liu, Y.-K., Li, Y.-F., Chen, X.-Y., Su, Z.-H., Zhang, X.-H., Ma, H.-L., & Fan, P. (2020). Sputtered and selenized Sb2Se3 thin-film solar cells with open-circuit voltage exceeding 500 mV. Nano Energy, 73, 104806. https://doi.org/10.1016/j.nanoen.2020.104806
17. Liu, X., Xiao, X., Yang, Y., Xue, D.-J., Li, D.-B., Chen, C., Lu, S., Gao, L., He, Y., Beard, M. C., Wang, G., Chen, S., & Tang, J. (2017). Enhanced Sb 2 Se 3 solar cell performance through theory-guided defect control. Progress in Photovoltaics: Research and Applications, 25(10), 861–870. https://doi.org/10.1002/pip.2900
18. Ma, Y., Tang, B., Lian, W., Wu, C., Wang, X., Ju, H., Zhu, C., Fan, F., & Chen, T. (2020). Efficient defect passivation of Sb 2 Se 3 film by tellurium doping for high performance solar cells. Journal of Materials Chemistry A, 8(14), 6510–6516. https://doi.org/10.1039/D0TA00443J


ISSN: 2181-3337 | SCIENTISTS.UZ

19. Mavlonov, A., Razykov, T., Raziq, F., Gan, J., Chantana, J., Kawano, Y., Nishimura, T., Wei, H., Zakutayev, A., & Minemoto, T. (2020). A review of Sb2Se3 photovoltaic absorber materials and thin-film solar cells. Solar Energy, 201, 227–246.
20. Moynihan, C. T., Gavin, D. L., & Syed, R. (1982). PRE-EXPONENTIAL TERM IN THE ARRHENIUS EQUATION FOR ELECTRICAL CONDUCTIVITY OF GLASS. Le Journal de Physique Colloques, 43(C9), C9-395-C9-398. https://doi.org/10.1051/jphyscol:1982975
21. Phillips, L. J., Savory, C. N., Hutter, O. S., Yates, P. J., Shiel, H., Mariotti, S., Bowen, L., Birkett, M., Durose, K., Scanlon, D. O., & Major, J. D. (2019). Current Enhancement via a TiO2 Window Layer for CSS Sb2Se3 Solar Cells: Performance Limits and High V oc. IEEE Journal of Photovoltaics, 9(2), 544–551. https://doi.org/10.1109/JPHOTOV.2018.2885836
22. Savory, C. N., & Scanlon, D. O. (2019). The complex defect chemistry of antimony selenide. Journal of Materials Chemistry A, 7(17), 10739–10744. https://doi.org/10.1039/C9TA02022E
23. Scheer, R., & Schock, H. (2011). Chalcogenide Photovoltaics. Wiley. https://doi.org/10.1002/9783527633708
24. Shiel, H., Hutter, O. S., Phillips, L. J., Swallow, J. E. N., Jones, L. A. H., Featherstone, T. J., Smiles, M. J., Thakur, P. K., Lee, T.-L., Dhanak, V. R., Major, J. D., & Veal, T. D. (2020). Natural Band Alignments and Band Offsets of Sb 2 Se 3 Solar Cells. ACS Applied Energy Materials, 3(12), 11617–11626. https://doi.org/10.1021/acsaem.0c01477
25. Shockley, W., & Queisser, H. J. (1961). Detailed Balance Limit of Efficiency of p-n Junction Solar Cells. Journal of Applied Physics, 32(3), 510–519. https://doi.org/10.1063/1.1736034
26. Streetman, B. G., & Banerjee, S. K. (2015). Solid State Electronic Devices. Pearson, 10(Pearson),596. https://books.google.co.uz/books/about/Solid_State_Electronic_Devices.html?id=-nnznQEACAAJ&redir_esc=y
27. Sze, S. M., & Ng, K. K. (2006). Physics of Semiconductor Devices (3rd ed.). Wiley. https://doi.org/10.1002/0470068329
28. Wang, L., Li, D.-B., Li, K., Chen, C., Deng, H.-X., Gao, L., Zhao, Y., Jiang, F., Li, L., Huang, F., He, Y., Song, H., Niu, G., & Tang, J. (2017). Stable 6%-efficient Sb2Se3 solar cells with a ZnO buffer layer. Nature Energy, 2(4), 17046. https://doi.org/10.1038/nenergy.2017.46
29. Wang, X., Li, Z., Kavanagh, S. R., Ganose, A. M., & Walsh, A. (2022). Lone pair driven anisotropy in antimony chalcogenide semiconductors. Physical Chemistry Chemical Physics, 24(12), 7195–7202. https://doi.org/10.1039/D1CP05373F
30. Wang, X., Tang, R., Wu, C., Zhu, C., & Chen, T. (2018). Development of antimony sulfide–selenide Sb2(S, Se)3-based solar cells. Journal of Energy Chemistry, 27(3), 713–721. https://doi.org/10.1016/j.jechem.2017.09.031
31. Wen, X., He, Y., Chen, C., Liu, X., wang, L., Yang, B., Leng, M., Song, H., Zeng, K., Li, D., Li, K., Gao, L., & Tang, J. (2017). Magnetron sputtered ZnO buffer layer for Sb2Se3 thin film solar cells. Solar Energy Materials and Solar Cells, 172, 74–81. https://doi.org/10.1016/j.solmat.2017.07.014
32. Wijesinghe, U., Longo, G., & Hutter, O. S. (2023). Defect engineering in antimony selenide thin film solar cells. Energy Advances, 2(1), 12–33. https://doi.org/10.1039/D2YA00232A
33. Williams, R. E., Ramasse, Q. M., McKenna, K. P., Phillips, L. J., Yates, P. J., Hutter, O. S., Durose, K., Major, J. D., & Mendis, B. G. (2020). Evidence for Self-healing Benign Grain Boundaries and a Highly Defective Sb 2 Se 3 –CdS Interfacial Layer in Sb 2 Se 3 Thin-Film Photovoltaics. ACS Applied Materials & Interfaces, 12(19), 21730–21738. https://doi.org/10.1021/acsami.0c03690
34. Zakutayev, A. (2017). Brief review of emerging photovoltaic absorbers. Current Opinion in Green and Sustainable Chemistry, 4, 8–15. https://doi.org/10.1016/j.cogsc.2017.01.002


ISSN: 2181-3337 | SCIENTISTS.UZ

35. Zhou, J., Xu, X., Duan, B., Wu, H., Shi, J., Luo, Y., Li, D., & Meng, Q. (2021). Regulating crystal growth via organic lithium salt additive for efficient Kesterite solar cells. Nano Energy, 89, 106405. https://doi.org/10.1016/j.nanoen.2021.106405
36. Zhou, Y., Leng, M., Xia, Z., Zhong, J., Song, H., Liu, X., Yang, B., Zhang, J., Chen, J., Zhou, K., Han, J., Cheng, Y., & Tang, J. (2014). Solution-Processed Antimony Selenide Heterojunction Solar Cells. Advanced Energy Materials, 4(8), 1301846. https://doi.org/10.1002/aenm.201301846
37. Zhou, Y., Wang, L., Chen, S., Qin, S., Liu, X., Chen, J., Xue, D.-J., Luo, M., Cao, Y., Cheng, Y., Sargent, E. H., & Tang, J. (2015). Thin-film Sb2Se3 photovoltaics with oriented one-dimensional ribbons and benign grain boundaries. Nature Photonics, 9(6), 409–415. https://doi.org/10.1038/nphoton.2015.78



ISSN: 2181-3337 | SCIENTISTS.UZ